Drop formation by DOD ink-jet nozzles: A comparison of experiment and numerical simulation

by T. W. Shield D. B. Bogy F. E. Talke

This paper presents a comparison of a numerical simulation of drop formation and ejection from a drop-on-demand (DOD) ink-jet nozzle with experimental observations from a particular nozzle-transducer design. In the numerical simulation, first the pressure waves in the transducer chamber are calculated using inviscid compressible flow theory to obtain the pressure history at the inner face of the nozzle plate. Then a viscous momentum integral computation is applied to the nozzle to obtain the velocity history at the outer face of the nozzle plate. Finally, the free surface shape is calculated using finite-difference methods on the one-dimensional equations for an inviscid incompressible free jet with surface tension that uses the nozzle exit velocity history as the driving boundary condition. The computations are compared with drop formation photographs

*Copyright 1987 by International Business Machines Corporation. Copying in printed form for private use is permitted without payment of royalty provided that (1) each reproduction is done without alteration and (2) the *Journal* reference and IBM copyright notice are included on the first page. The title and abstract, but no other portions, of this paper may be copied or distributed royalty free without further permission by computer-based and other information-service systems. Permission to *republish* any other portion of this paper must be obtained from the Editor.

obtained from a particular nozzle-transducer design. Encouraging agreement is obtained, but the numerical model will require added sophistication before detailed agreement can be expected.

1. Introduction

In this paper a numerical simulation of the drop formation in drop-on-demand (DOD) ink-jet printer devices is described. Bogy and Talke [1] deduced that the pressure at the inner face of the nozzle plate of a squeeze-tube ink-jet transducer is due to the constructive interference of acoustic pressure waves created in the fluid cavity by the expansion and contraction of the piezoelectric sleeve that surrounds the glass lining of this type of nozzle. This is in contrast to the incompressible model presented by Beasley [2] to explain the fluid mechanics inside the transducer chamber.

In [3] we presented two numerical solutions for the drop formation process outside the nozzle that are based on one-dimensional jet theories, one with and one without radial inertial effects. These models are for inviscid fluids with surface tension, and they require an axial velocity boundary condition at the outside face of the nozzle plate. These schemes use a Eulerian formulation. A numerical solution for the drop formation outside of the nozzle based on one-

dimensional equations without radial inertia and with a Lagrangian formulation was presented by Adams and Roy [4]. This free surface drop formation problem was also considered by Fromm [5], who used a numerical solution of the axisymmetric Navier-Stokes equations.

In our previous work an artificial pressure history inside the nozzle plate was used with a momentum integral method through the nozzle to obtain the nozzle exit velocity boundary condition for the free surface jet problem.

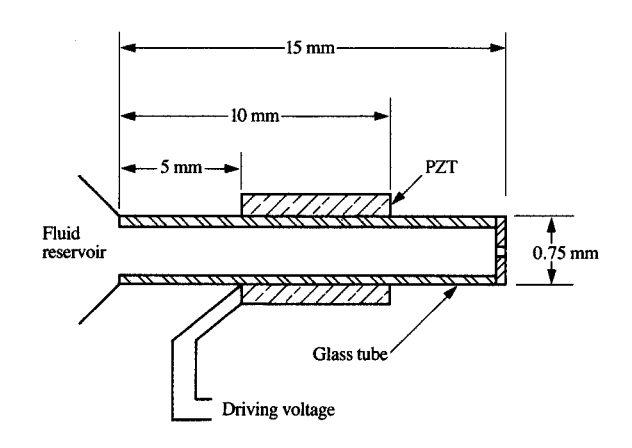
The purpose of the present paper is to combine the calculations in the three regions of the ink-jet device to allow prediction of drop behavior that can be compared with experiments. First, in Section 2, an experimental apparatus is described and experimental results showing drop formation and ejection at various instants during the process are presented for water and ethylene glycol under various driving conditions. Next, in Section 3, the acoustics inside the transducer cavity are described using a method of characteristics in a manner similar to that used for analyzing pressure transients in pipes (water-hammer analysis). This yields the pressure history at the inside of the nozzle plate that results from the expansion and contraction of the piezoelectric tube. Then, this pressure history is used in the nozzle momentum integral equations to predict the velocity outside the nozzle plate. Finally, this velocity boundary condition is used with the numerical solution for the free jet equations to predict the drop formation process leading to drop size and velocity. In the last section, Section 4, the numerical predictions are compared with the experimental observations, and some comments are made concerning the limitations of the numerical simulator and the need for further work.

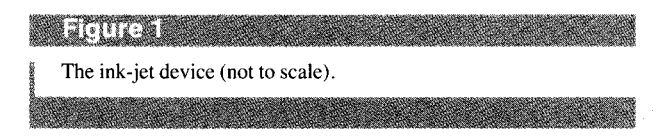
2. Experimental observations

• The apparatus and its operation

The experimental apparatus consists of a nozzle transducer, an electronic driver, and a video system. The transducer has a fluid cavity that is composed of a glass tube surrounded by a piezoelectric cylinder over a portion of its length. One end of the tube is closed off by a thin silicon plate that contains a small orifice, about 50 micrometers in diameter. The other end of the tube is connected by a larger-diameter tube to a fluid reservoir. The dimensions of the device are shown in **Figure 1**.

The nozzle is driven by periodic rectangular pulses at a fixed frequency around 1 kHz. By using a strobe light it is possible to view the formation of the drops with a television camera equipped with a microscope lens. The drop formation is viewed at various times by using a variable delay between the driving pulse and the strobe flash. As the delay is increased, the effect is to produce a slow-motion picture of the formation of the drop. Since the drop formation process is extremely repeatable, even down to the





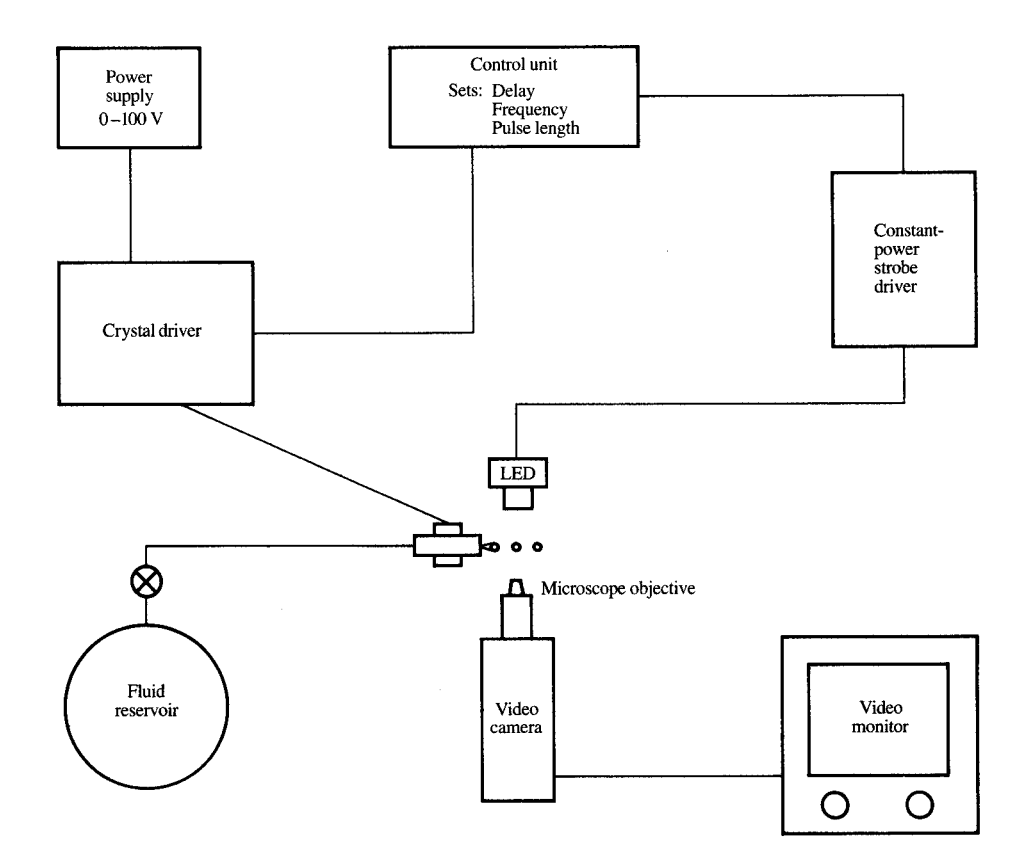
smallest detail, this technique provides a smooth, stable picture of the drop evolution.

A block diagram of the electronic equipment used to control the experiment is shown in Figure 2. The main control unit allows control of frequency, pulse length, and strobe delay. The light source of the strobe is a LED that is driven by a constant power source. Its intensity does not vary with the pulse length or frequency. The driver for the piezoelectric crystal uses a logic-level signal from the main control unit to modulate the output of the high-voltage power supply. The television camera is a high-sensitivity black and white commercially available closed-circuit camera, which is directly connected to a TV monitor. The lens is a standard microscope lens that is screwed into an adjustable-length microscope nosepiece. Typically, a 10× microscope objective lens is used. Although higher-power objectives would show more detail, they require more light and hence do not give a clear picture.

The drop transducer is mounted so that it can be moved vertically and horizontally to allow different parts of the drop stream to be viewed. The drop transducer is connected to the fluid reservoir by a plastic tube which allows the reservoir to be fixed, keeping its free surface at the approximate elevation of the nozzle exit so that static pressure does not tend to drive the fluid out of the nozzle. Leaking of fluid would wet the nozzle face and make it impossible for well-formed drops to be produced.

The device must be carefully primed to remove all air from the chamber, since air bubbles in the chamber absorb the pressure waves produced by the piezoelectric crystal and prevent a drop from forming. It is usually advisable to start with fluids such as water or alcohol, which wet surfaces





Block diagram of experimental apparatus.

better than ethylene glycol, and then to switch fluids after the chamber is free from air bubbles. In order to prime the device the fluid reservoir can first be pressurized with air to approximately 6 to 9 psi to force fluid through the orifice.

The optimum pulse length for driving the device can be determined experimentally by observing the breakup of a continuous, pressurized jet. Since this particular transducer design relies on the constructive interference of pressure waves, caused by the rise and fall of the driving pulse to eject the drops, the pulse length is the critical parameter for proper drop ejection. The easiest way to find the optimum pulse length (the "tuned" or resonance pulse length) is to adjust it for the shortest-length breakup of the continuous jet, since it is at this condition that the pressure pulse at the nozzle is the strongest.

The best driving voltage can also be found during continuous-jet operation simply by increasing the voltage until the jet breaks up reasonably close to the nozzle.

The experimental results are presented in the next section in the form of drop shapes at various times during the drop formation and ejection process. The main control unit directly displays the strobe delay time in microseconds, thereby providing convenient timing of the drop profiles. It is possible to measure the distance the drop travels in a given time interval; however, the drop velocity is not constant until after the drop has separated from the nozzle and has become spherical. Thus, this method is only suitable for average velocity measurements. The parameters, corresponding to the numerical simulation, are the pulse length, driving voltage, and choice of fluid.

• Experimental results

The experimental results are presented as a sequence of photographs taken directly from the video monitor by use of an oscilloscope camera. Two different fluids were used, ethylene glycol and water, because of their material properties and because they are commonly used as the base fluids for inks in ink-jet printing. Their surface tensions are not very different, but their viscosities are quite different, and they are observed to behave quite differently in our experiment. The physical properties of the two fluids and some other parameter values are listed in **Table 1**. A summary of the conditions for the photographs presented in the figures is given in **Table 2**.

The photographs were taken at 30-µs time intervals. The driving voltage needed to eject the drops varied greatly depending on the fluid and pulse length. The ethylene glycol needed a higher driving voltage than the water.

Figure 3 shows a low-magnification picture of the nozzle end and a sequence of three equally spaced droplets after ejection from the nozzle. Figures 4(a)-4(d) show four sequences of drop formation and ejection for ethylene glycol. All times mentioned are from initial pulse rise. In Figure 4(a) the pulse length is 10 μ s, the shortest pulse-length resonance condition, and the pulse amplitude is 90 volts. Here the time of the first photograph is at 30 μ s. The sequence shows that the drop forms without a satellite drop and detaches after about 120 μ s. A second positive pressure pulse, which results from a reflection, occurs at 90 µs. In Figure 4(b) the pulse length is 15 μ s, which does not establish a resonance condition, and the pulse amplitude is 70 volts. Again, the first photograph was taken at 30 μ s. Although drops are ejected under these conditions, a comparison of Figures 4(a) and 4(b) shows that the drops are smaller in the latter case and two drops are formed in place of one. This is explained in the next section when the numerical model is discussed. In Figure 4(c) the pulse length is 20 µs, twice the resonance pulse length, and the pulse amplitude is 70 volts. The first photograph is taken at 30 μ s, and the sequence appears to be very similar to that in Figure 4(a). It may be somewhat surprising that the second resonance condition requires a lower pulse amplitude than the first one to obtain similar drop ejection. This can also be explained when the numerical solution is discussed. Figure 4(d) shows another drop sequence for a 20-μs pulse length, but with a pulse amplitude of 90 volts, as in Figure 4(a). The first photograph here is at 60 μ s [the photograph at 30 μ s is the same as in Figure 4(a)], and an overdriven condition is evident, with a satellite drop being formed.

Figures 5(a)-5(d) show four sequences of drop formation and ejection for water. Here it is observed that the drop formation process is not as well controlled as for ethylene glycol. In Figure 5(a) the pulse length is $10 \mu s$, the shortest pulse-length resonance condition, and the pulse amplitude is 55 volts, as compared to 90 volts in Figure 4(a) for ethylene

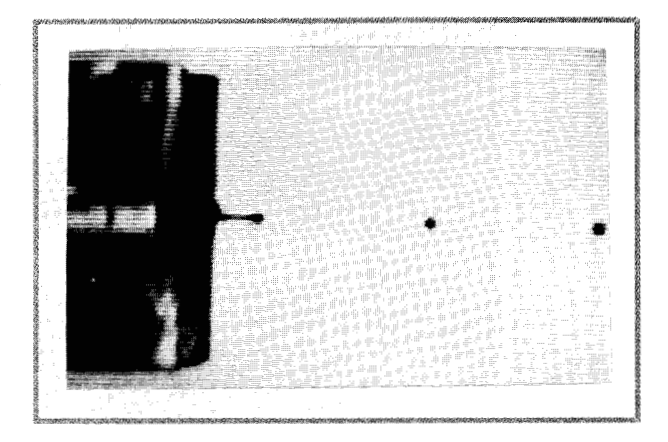


Figure 3

Low-magnification view of ink-jet nozzle ejecting a series of drops.

Table 1 Typical values of some physical parameters that characterize ink-jet printing.

	Ethylene glycol	Water	
Density (g/cm³)	1.02	0.997	
Surface tension (g/s ²)	60.0	65.0	
Viscosity (g/(s·m))	3.0	0.89	
Other parameters			
Nozzle diameter, a	50.0 μm		
Reference velocity, V_0	1.0 m/s		
Reference time, a/V_0	50.0 μs		

Table 2 The driving voltage applied at each pulse length for the two fluids used in the experiments along with a conversion table from microseconds to the nondimensional time.

Water			
Pulse length	Driving voltage		
10.0	55.0		
15.0	45.0		
20.0	45.0, 55.0		
25.0	50.0		
Ethylene glycol			
Pulse length	Driving voltage		
10.0	90.0		
15.0	70.0		
20.0	70.0, 90.0		
Time in	Nondimensional		
microseconds	time		
30.0	0.60		
60.0	1.20		
90.0	1.80		
120.0	2.40		
150.0	3.00		
180.0	3.60		

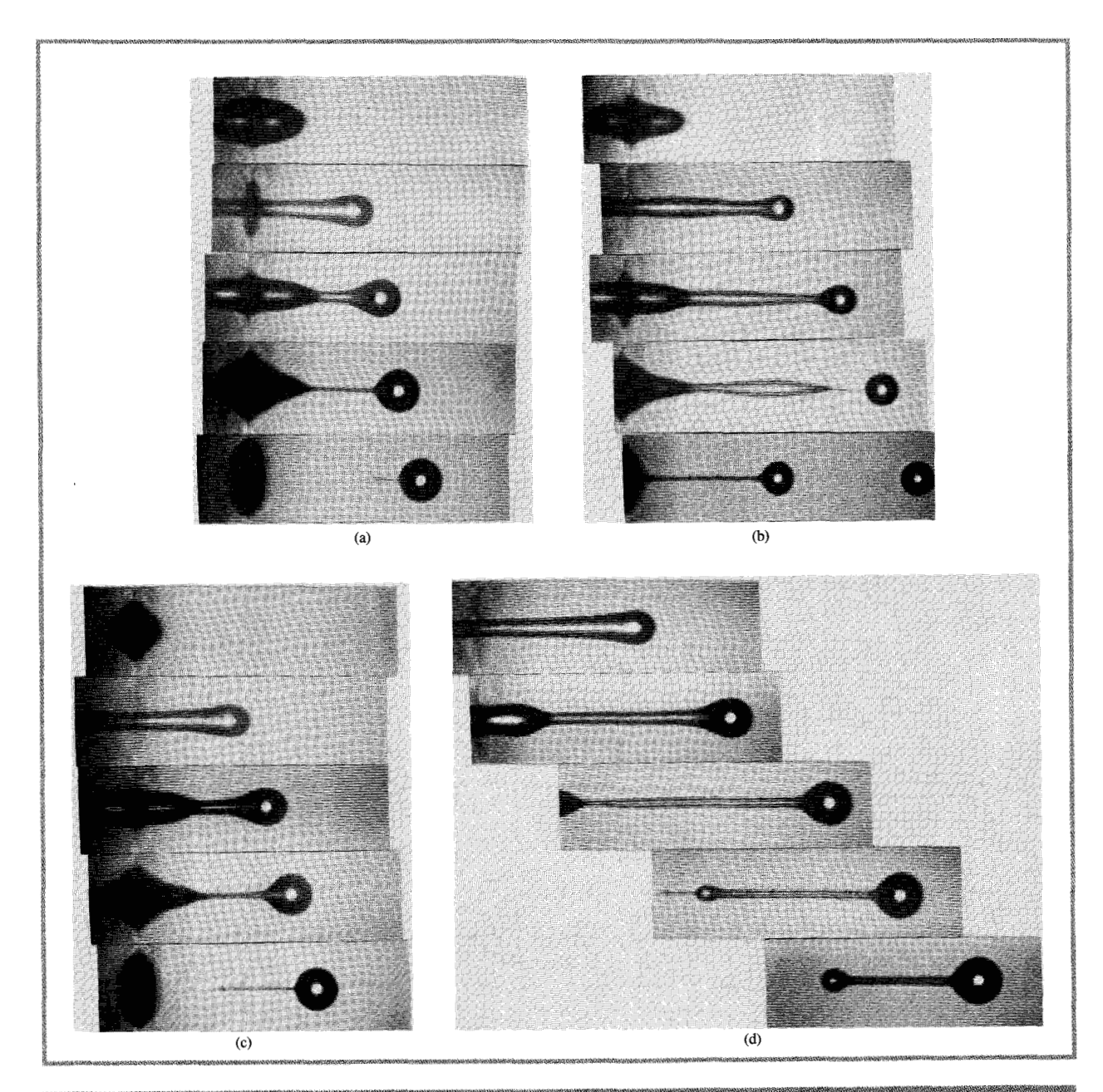


Figure 4

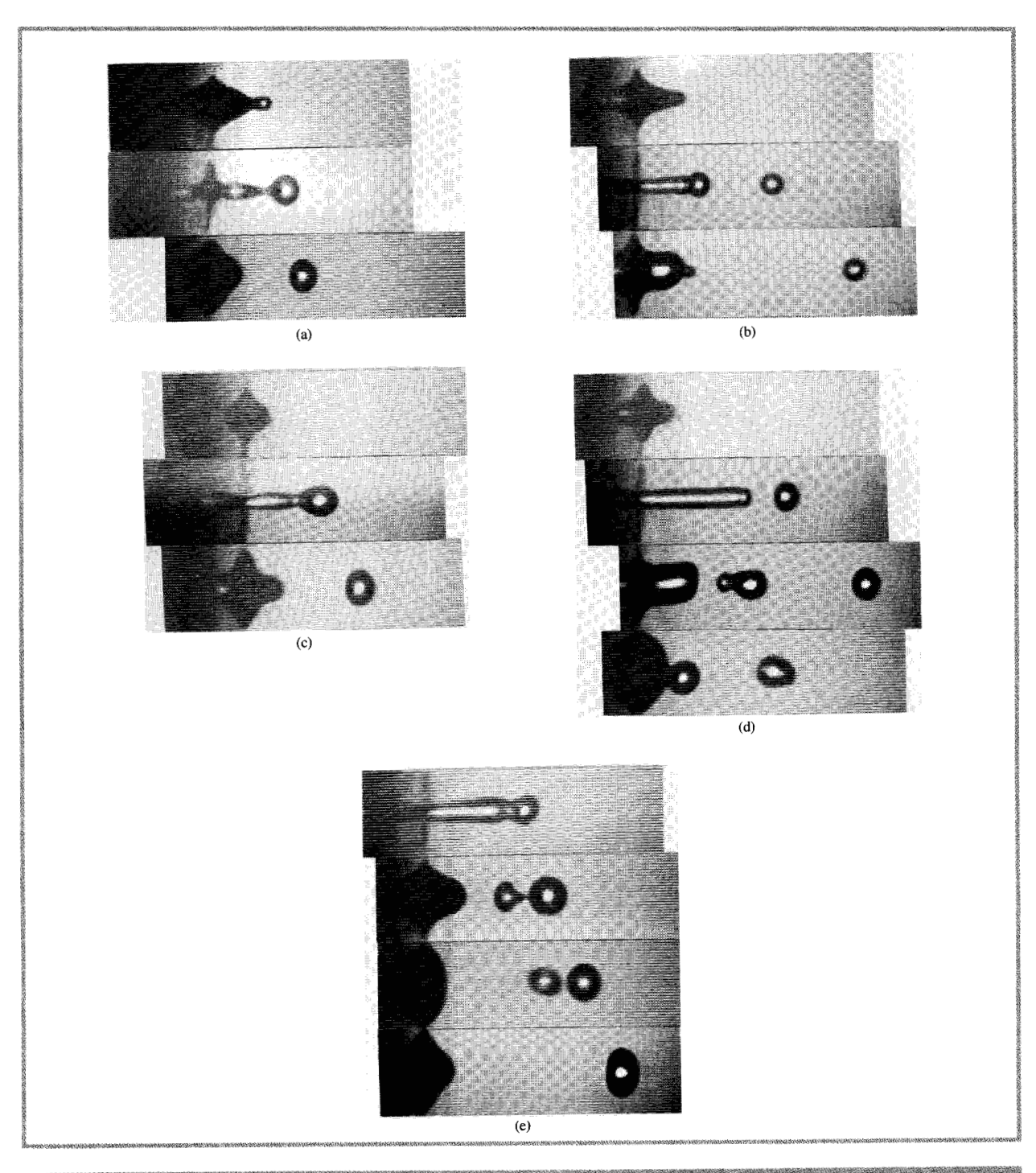
Ethylene glycol ejected by a pulse of (a) 90.0 V for $10.0 \text{ }\mu\text{s}$; (b) 70.0 V for $15.0 \text{ }\mu\text{s}$; (c) 70.0 V for $20.0 \text{ }\mu\text{s}$; and (d) 90.0 V for $20.0 \text{ }\mu\text{s}$.

glycol. A clean drop is formed without satellites. In Figure 5(b) the pulse length is 15 μ s, not a resonance condition, and the pulse amplitude is only 45 volts. As in the case of ethylene glycol in Figure 4(b), the drops are smaller for 15 μ s in Figure 5(b) than for the 10- μ s pulse length in Figure 5(a). In this case the second drop does not separate, but is recaptured by the meniscus at the nozzle.

In Figure 5(c) the pulse length is 20 μ s and the pulse amplitude is 45 volts, causing well-formed drops to be ejected without satellites. In Figure 5(d) the pulse length is

maintained at 20 μ s, but the driving voltage is raised to 55 volts. This causes an overdriven condition and a somewhat erratic drop formation process.

The sequences of drop formation pictures for both ethylene glycol and water show some similar characteristics. Both show good operation at the fundamental and first harmonic pulse lengths, and both show that multiple small drops are formed at the intermediate pulse length. Also, both show that overdriving leads to satellite formation at resonance pulse lengths.



Figure

Water ejected by a pulse of (a) 55.0 V for 10.0 µs; (b) 45.0 V for 15.0 µs; (c) 45.0 V for 20.0 µs; (d) 55.0 V for 20.0 µs; and (e) 50.0 V for 25.0 µs.

3. Numerical simulation

The first step in the numerical simulation is to derive the pressure history at the nozzle end of the chamber due to the expansion and contraction of the chamber walls resulting from the application of a rectangular voltage pulse to the piezoelectric sleeve. The response of the piezoelectric crystal tube itself was studied in Bugdayci et al. [6], in which the inner cylindrical wall displacement of the tube was

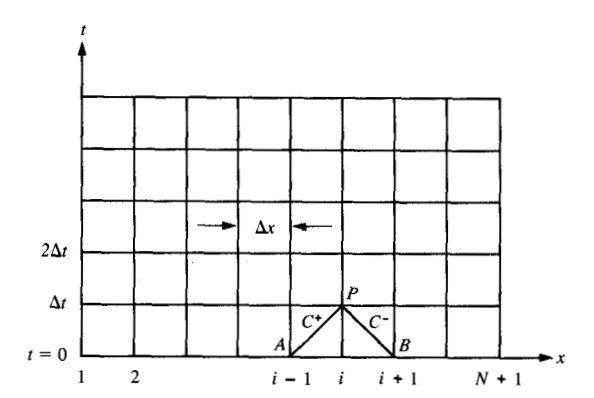


Figure 6

The discretization used for the method of characteristics calculation of the pressure waves in the device chamber.

calculated for an applied voltage step. In this analysis we make the simplifying assumption that the expansion and contraction of the transducer chamber follows that of the piezoelectric sleeve, and it is also linearly proportional to the applied voltage step. We leave this proportionality constant undetermined so that there remains a free parameter in the solution, which can be used to match the final drop velocities obtained from the experiment and computation.

• Pressure history calculation at the inner nozzle face
Pressure transients inside deformable pipes have been
studied extensively in water-hammer analysis for piping
systems. A nonlinear form of the one-dimensional
continuity equation for compressible flow in elastic pipes
with linearly varying diameters is derived in Chapter 17 of
Streeter and Wylie [7]. This equation can be written in the
form

$$p_t + \rho a^2 u_x + u p_x + 2\rho a^2 \beta u / D = 0,$$
 (1)

where p(x, t) and u(x, t) are the pressure and velocity functions, ρ is the density, assumed constant, a is the wave speed in the elastic pipe, D(x, t) is the pipe inner diameter, and β is the slope of the undeformed pipe diameter. Subscripts denote partial differentiation. The wave speed, a, depends on the fluid and the wall properties, and is given by

$$a = c \left[1 + \rho c^2 \left(\frac{Dc_1}{Ee} \right) \right]^{-1/2}, \tag{2}$$

where E is Young's modulus, e is the pipe wall thickness, c is the acoustic wave speed in the fluid, and c_1 equals $(1 - \sigma/2)$, $(1 - \sigma^2)$, or 1 (where σ is Poisson's ratio of the pipe), depending on whether the pipe is anchored at its upstream end only, is anchored throughout against axial movement, or

is anchored with expansion joints throughout. The expansion of the pipe due to the internal pressure is ignored; hence D is a function of x only in this analysis.

A one-dimensional momentum equation with frictional drag based on the Darcy-Weisbach equation is also derived in [7], and it has the form

$$p_x + \rho(u_x + uu_y) + \rho f u |u|/2D = 0.$$
 (3)

The friction factor is obtained from a force balance on a fixed length of pipe with steady flow producing a viscous drag. For the short time scales in our application, the friction factor has very little effect on the solution and was ignored in our calculations.

The method of characteristics provides a convenient approach for solving (1) and (3). The corresponding characteristic equations are derived in [7] and have the form

$$\frac{1}{\rho a} p_t + u_t + \frac{2a\beta}{D} u + \frac{fu |u|}{2D} = 0, \tag{4}$$

$$\frac{dx}{dt} = u + a, \quad \text{on } C^+, \tag{5}$$

$$-\frac{1}{\rho a}p_{t} + u_{t} - \frac{2a\beta}{D}u + \frac{fu|u|}{2D} = 0,$$
 (6)

$$\frac{dx}{dt} = u - a; \quad \text{on } C^-, \tag{7}$$

where the C^+ and C^- characteristic lines in the x-t plane are defined by (5) and (7), and they are curved lines since u is a function of x and t. This set of characteristic equations can be put in finite difference form and then solved numerically, as described in [7]. The use of these nonlinear equations is necessary in very flexible tubes where the wave speed, a, is of the same order of magnitude as the fluid velocity, u. For application to pressure transients in the ink-jet transducer of interest in this study, the channel walls are made of glass and piezoelectric ceramic, which have relatively high elastic moduli, so that the wave speed, a, does not fall much below 1500 m/s. On the other hand, the drop velocity is observed to be between 3 and 5 m/s. Therefore, it is reasonable to expect that $u \ll a$ in (5) and (7), and so only small errors will result from neglecting u in these equations. If this is done, the characteristics become straight lines in the x-t plane with slopes $\pm a$. We make this approximation here for convenience of analysis, and therefore we replace (5), (7) by

$$\frac{dx}{dt} = a$$
 on C^+ , $\frac{dx}{dt} = -a$ on C^- . (8)

This is tantamount to using linear acoustics except for the viscous drag term.

Next the finite-difference solution of the characteristic equations for the transducer cavity shown in Figure 1 is briefly described. Divide the pipe section into N increments Δx in length, as shown in **Figure 6**. The time step is computed from

$$\Delta t = \Delta x/a \tag{9}$$

so that the first of (8) is satisfied by the line AP in Figure 6. If u and p are known at point A, then (4), which is valid along C^+ , can be integrated between A and P to relate u_p , p_p to u_A , p_A . Likewise, integration along C^- is used to relate u_p , p_p to u_B , p_B . In terms of the index i in Figure 6, we can write these two equations as

$$C^{+}: p_{P_{i}} = C_{P} - KBu_{P_{i}}, \tag{10}$$

$$C^-: p_P = C_M + KBu_P, \tag{11}$$

where C_P and C_M are along C^+ and C^- , respectively, and are given by

$$C_P = p_{i-1} + KBu_{i-1} - \frac{LR}{D_{i-1}}u_{i-1} |u_{i-1}| - \frac{MB}{D_{i-1}}u_{i-1}, \qquad (12)$$

$$C_{M} = p_{i+1} - KBu_{i+1} + \frac{LR}{D_{i+1}}u_{i+1}|u_{i+1}| - \frac{MB}{D_{i+1}}u_{i+1}, \qquad (13)$$

with

$$KB = \rho a$$
, $LR = \rho f \Delta x/2$, $MB = 2a\rho \beta \Delta x$. (14)

Solving (10) and (11), we obtain

$$p_{P_i} = (C_P + C_M)/2, \qquad u_{P_i} = (p_{P_i} - C_M)/2.$$
 (15)

When p and u are known at the present time step, we can advance to the next time step at the interior points. In order to update the values of p and u at the end points of the chamber, we must make use of the boundary conditions. For the nozzle end it is assumed that the orifice is small compared to the chamber cross section, and therefore we invoke a closed-end boundary condition and use (10) and (12) to obtain

$$u_{P_{N+1}} = 0, p_{P_{N+1}} = C_P.$$
 (16)

At the inlet end we assume that a reservoir pressure p_r prevails, and with this (11) and (13) yield

$$p_{P_r} = p_r, \qquad u_{P_r} = (p_r - C_M)/KB.$$
 (17)

Finally, initial conditions at t = 0 (the pulse rise time) and jump conditions at $t = t_n$ (the pulse fall time) must be specified. It is assumed that an instantaneous pressure $p_0(x)$ results from the response of the piezoelectric tube. The pressure per volt was determined in Bugdayci et al. [6] under the assumption of uniform conditions along its length. It was also found there that for the PZT (ceramic piezoelectric) tubes in use, a positive voltage step at the outer electrode caused the inside diameter of the tube to increase, leading to an initial pressure drop. The pulse length, t_p , is an important design parameter for nozzle operation, as shown in Bogy and Talke [1]. After the time interval t_n , the voltage is dropped back to zero, causing a contraction of the tube and adding a corresponding pressure jump at that instant. A new set of pressure waves is thereby superimposed on those remaining from the initial voltage step. Therefore, the initial conditions are

$$p_i(x, 0^+) = -p_0(x), \quad u(x, 0^+) = 0.$$
 (18)

Then at time $t = t_n$ the jump conditions are

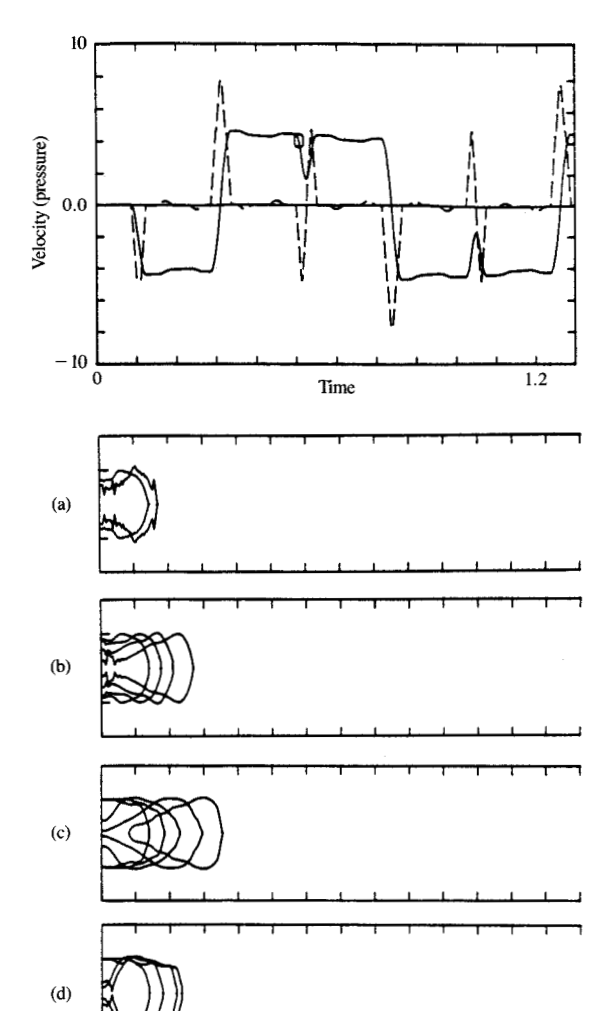
$$p(x, t_n^+) = p(x, t_n^-) + p_0(x), \quad u(x, t_n^+) = u(x, t_n^-).$$
 (19)

The function $p_0(x)$ representing the axial distribution of pressure resulting from the voltage step is unknown. In the present application we assume a uniform value over the region of the piezoelectric sleeve with a linear ramp to zero near the ends of the sleeve.

A FORTRAN program was written to implement the solution presented here for the nozzle chamber in Figure 1. The resulting histories at the inner face of the nozzle plate are shown for various pulse lengths as dashed lines in Figures 7-10. These figures show that the first disturbance is the negative pressure resulting from the initial expansion of the piezoelectric sleeve. The first positive pressure pulse to arrive at the nozzle is the reflection from the reservoir end of the chamber of the initial pressure pulse caused by the expansion of the crystal, which may be reinforced when the voltage drops and the piezoelectric sleeve contracts at $t = t_p$. In Figure 7, where t_n is 10 μ s, near the lowest resonance pulse length (which is $10.4 \mu s$), reinforcement does occur, producing a double-amplitude pressure pulse. This illustrates the tuning that occurs when the pulse length is chosen to match the chamber length. In Figure 8, where t_n is 15 μ s, which is not a resonance condition, the two positive pulses arrive at different times and no reinforcement occurs. In Figure 9, t_n is 20 μ s, which is near the second resonance condition; thus the pressure rise due to the contraction of the crystal reinforces the pressure pulse caused by the initial expansion of the crystal after it has reflected from both the nozzle and the reservoir ends of the chamber. In Figure 10, t_p is 25 μ s, and the pressure pulses arrive at separate times without reinforcing each other.

 Velocity history calculation at outer nozzle face The numerical schemes we developed in [3] for drop formation require a velocity boundary condition at the outer nozzle face. An equation based on momentum integral techniques was derived in that paper that relates this velocity to the pressure history at the inner nozzle face. This derivation involves several assumptions: 1) The velocity profile has an assumed dependence on the radial coordinate r that satisfies the viscous no-slip boundary condition inside the nozzle. 2) The flow is assumed to be incompressible; i.e., the volume flow rate Q is a function of t only. 3) The entrance flow comes from such a large section that no work is required in this section to accelerate the fluid into the nozzle. 4) The outer flow back pressure is negligible. 5) The fluid is Newtonian, and 6) the fluid always completely fills the nozzle region which is taken as the control volume. The equation obtained for determining the nondimensional volume velocity Q is

$$Q_t + \frac{5.784}{bR}Q = \pi^2 b^2 P(t)/L,$$
 (20)



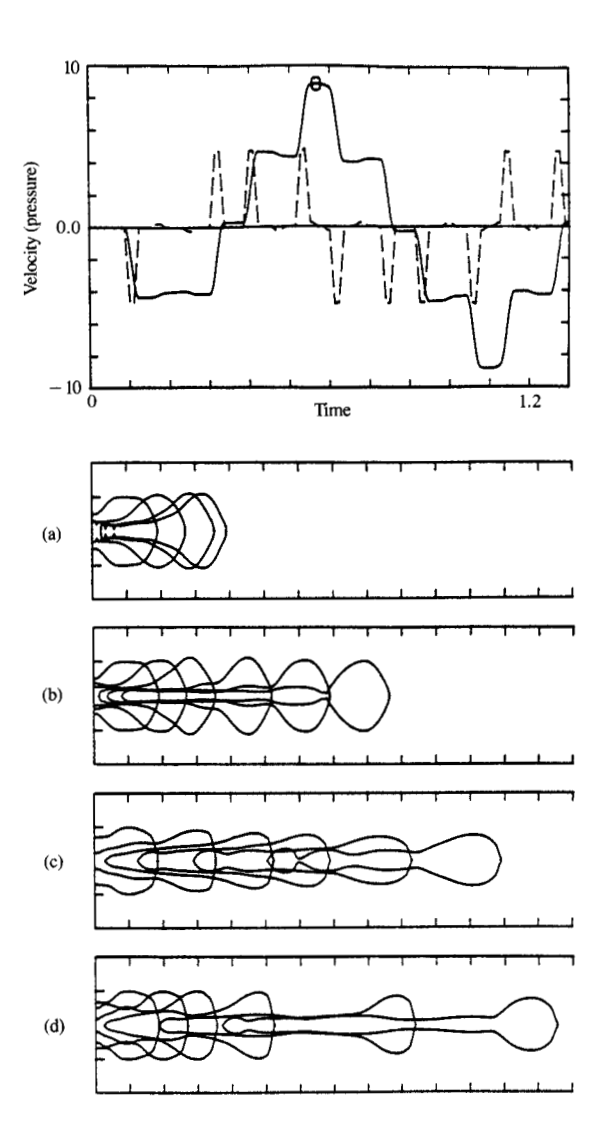


Figure 7

Calculations with a pulse length of $10.0~\mu s$ for (a) Scheme A, W=1.0; (b) Scheme A, W=5.0; (c) Scheme B, W=1.0; and (d) Scheme B, W=5.0.

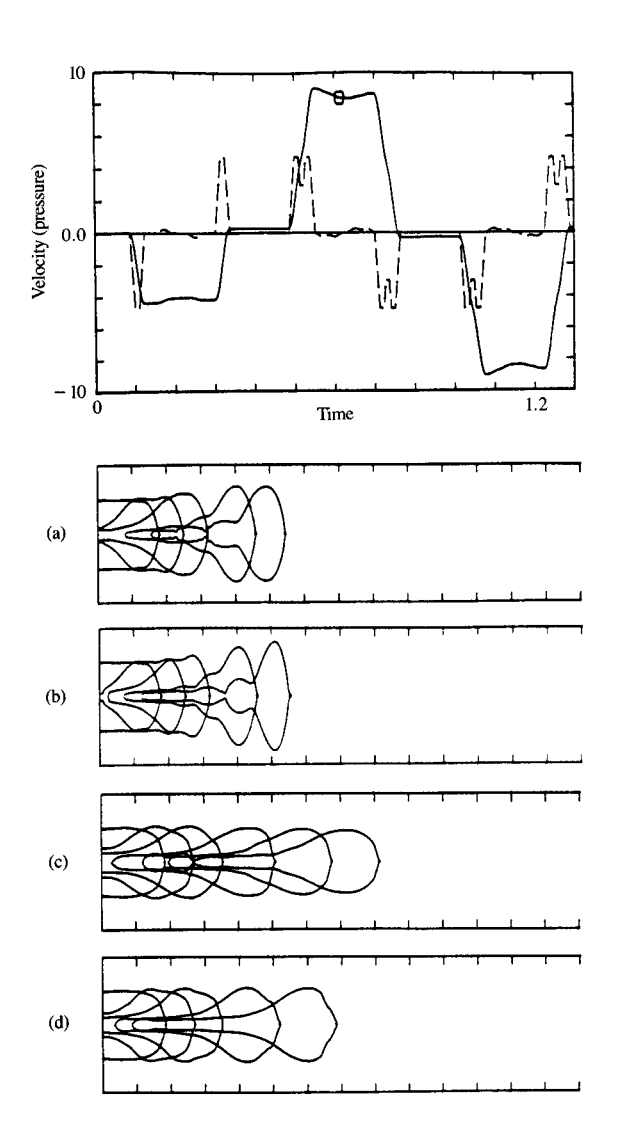
Figure 8

Calculations with a pulse length of 15.0 μ s for (a) Scheme A, W=1.0; (b) Scheme A, W=5.0; (c) Scheme B, W=1.0; and (d) Scheme B, W=5.0.

in which the numerical constant is a shape parameter obtained from integrating the assumed flow profile function of r. R is the Reynolds number based on the nozzle exit radius and a reference velocity of the flow, and has a value of about 2.5. The nozzle is assumed to be conical with length L, inner radius b, and outer radius of 1. P(t) is the driving pressure history at the inner nozzle face, which is assumed to be known.

In our previous work the driving pressure was an assumed analytical form that allowed (20) to be solved in closed form. In the present work the pressure is obtained from the numerical solution of the characteristic equations described

in (1)–(19) and is presented in Figures 7–10, so (20) must be numerically solved with a simple trapezoidal integration scheme. Also appearing in Figures 7–10 are the volume velocity histories corresponding to these pressure histories. The velocity units are to be discussed presently. In Figure 7 the maximum velocity amplitude is slightly more than four dimensionless units. In Figures 8–10 it reaches about eight. From these figures the relationship between the pressure history at the inside nozzle face to the velocity history at the outside nozzle face is revealed as almost an integral one, which implies that the second term in (20) is not very important in the calculation.



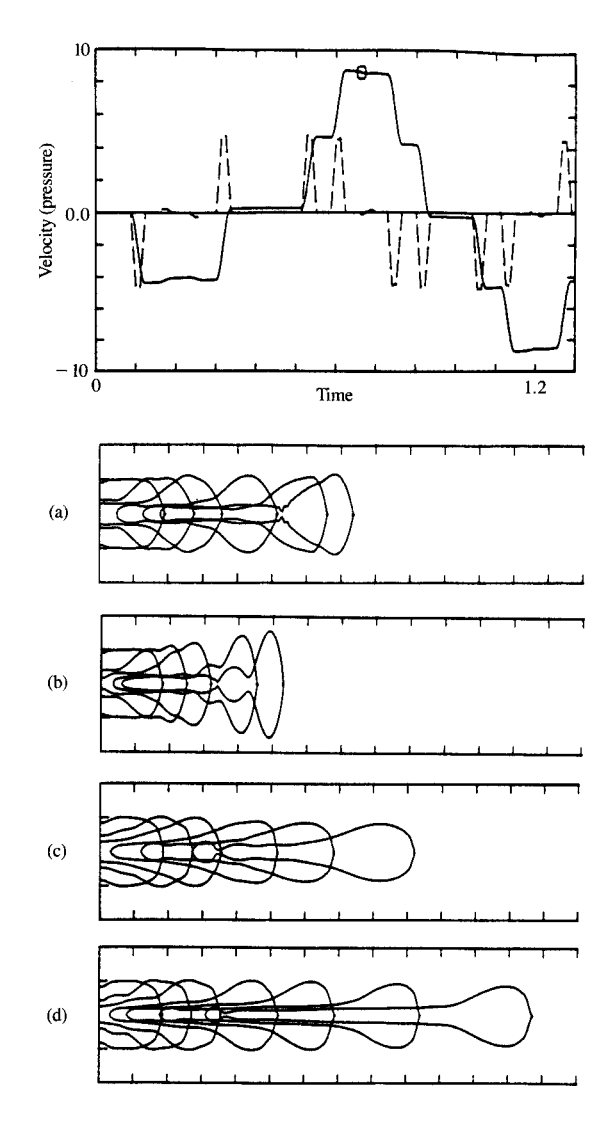


Figure 9

Calculations with a pulse length of $20.0 \mu s$ for (a) Scheme A, W = 1.0; (b) Scheme A, W = 5.0; (c) Scheme B, W = 1.0; and (d) Scheme B, W = 5.0.

• Drop formation calculations

The numerical schemes we developed can now be used with the velocity history just obtained, which provides the required boundary condition. Two schemes, called Scheme A and Scheme B, were presented in our previous paper. Scheme A is more complicated and includes effects of radial inertia, whereas Scheme B is simpler since it neglects the radial inertial effects. Both schemes have a single parameter, the Weber number, W, defined by

$$W = \rho r_0 V_0^2 / T, \tag{21}$$

where T is the surface tension of the fluid and r_0 is the exit radius of the nozzle. The value of the Weber number can

Figure 16

Calculations with a pulse length of 25.0 μ s for (a) Scheme A, W=1.0; (b) Scheme A, W=5.0; (c) Scheme B, W=1.0; and (d) Scheme B, W=5.0.

either be prescribed, thus determining the reference velocity V_0 for a given fluid, or it is determined from a chosen reference velocity. If the reference velocity is chosen as the capillary wave speed of a given fluid, then the Weber number is unity for that fluid. The other possible choice for the reference velocity comes from the boundary conditions. Choosing the nondimensional amplitude of the exit velocity amounts to picking the reference velocity. By comparing the computation to the experiments, we can determine V_0 to force agreement of the final velocities.

Another parameter in the numerical simulation is the time t_0 at which the free surface flow calculations can begin relative to the initial rise of the pressure pulse. Since the

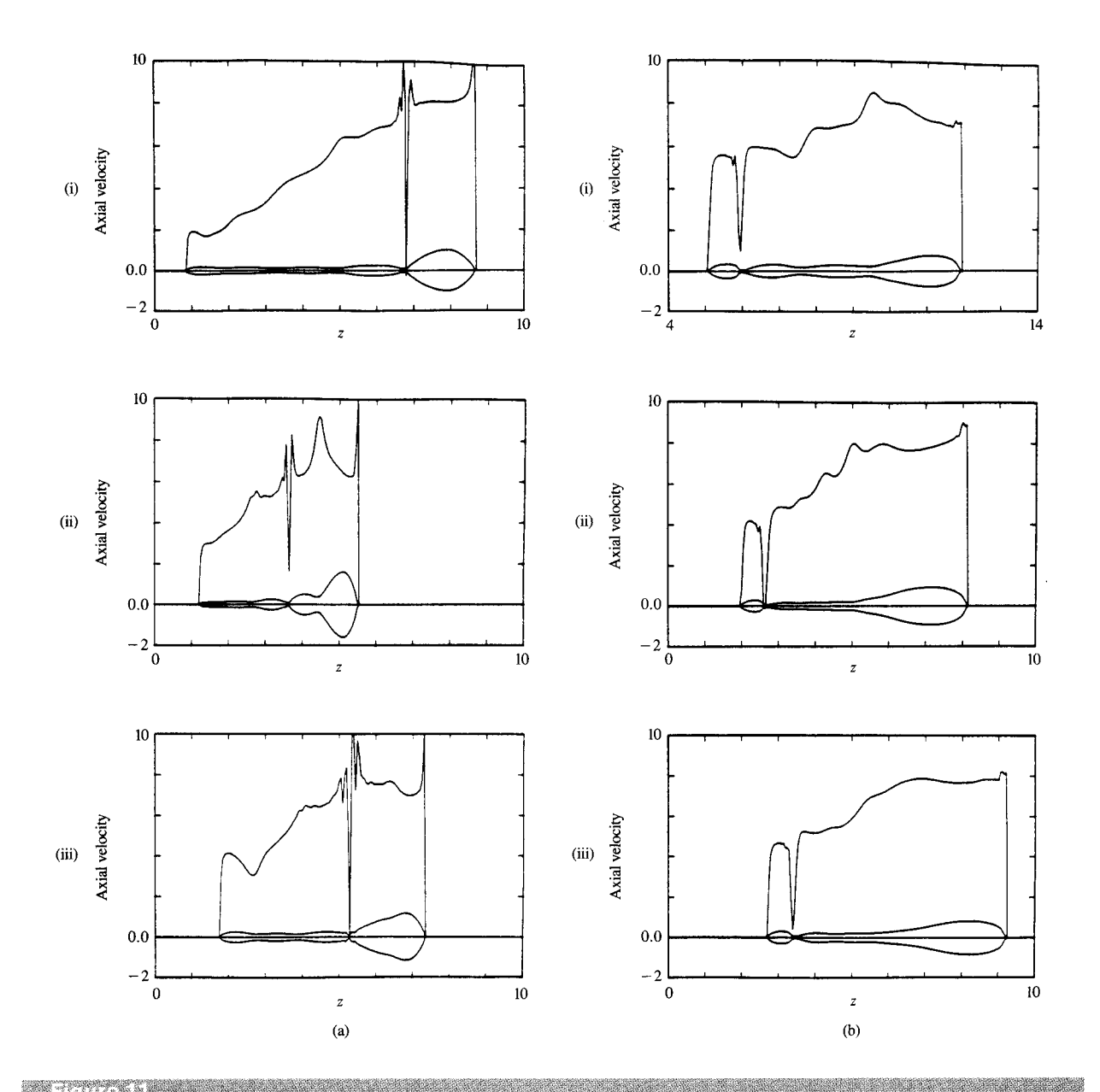
Table 3 Nondimensional times at which drop profiles are shown for the combinations of parameters used. W is the Weber number and t_0 is the pulse length in microseconds. The number in parentheses is the index at which breakoff occurred.

SCHEME A ($\Delta t = 0.001$, $\Delta z = 0.05$) $t_{-} = 25.0$			20	0	15	0	1	0.0
p = 0 =	0.66		20.0 0.61		15.0 0.57		10.0 0.51	
W =	1.0	5.0	1.0	5.0	1.0	5.0	1.0	5.0
	0.76	0.76	0.71	0.71	0.67	0.67	0.61	0.61
	0.86	0.86	0.81	0.81	0.77	0.77	0.678	0.71
	0.96	0.96	0.91	0.837 (4)	0.802 (5)	0.87		0.81
	1.052 (4)	1.045 (4)	1.053 (4)	0.91	0.87	1.006 (4)		0.968 (-)
	1.16	1.16	1.062	1.11	0.914	1.07		. ,
	1.467	1.289	1.084	1.164		1.27		
						1.482		
SCHE.	$ME B (\Delta t = 0.0$	$01, \Delta z = 0.05)$						
_ =	25	0.0	20.0		15.0		10.0	
p =	= 0.66		0.61		0.57		0.51	
W =	1.0	5.0	1.0	5.0	1.0	5.0	1.0	5.0
	0.76	0.76	0.71	0.71	0.67	0.67	0.61	0.61
	0.86	0.86	0.81	0.81	0.77	0.77	0.71	0.71
	0.96	0.96	0.91	0.91	0.87	0.87	0.81	0.81
	1.107 (5)	1.109 (7)	1.053 (5)	1.068 (8)	1.015 (5)	0.994 (5)	1.01	0.851(-)
	1.16	1.16	1.11	1.11	1.07	1.07	1.055 (4)	
	1.36	1.36	1.31	1.31	1.27	1.27	1.21	
	1.657	1.66	1.479		1.57	1.57		
		2.054			1.945	2.07		
		Recalculation with a different t_0				Recalci with twice the d		
		$t_{\rm p} = 25.0$				t _p =	10.0	
		$t_0^{\nu} = 0.61$				$t_0 =$	0.51	
		$\check{W} = 5.0$				W =	5.0	
	Scheme	A	В		Scheme	A		В
		0.71	0.71	1		0.61		0.61
		0.81	0.81			0.71		0.71
		0.91	0.91			0.81		0.802 (6)
		1.045 (4)	1.11			0.906 (4))	0.802 (0)
		1.11		30 (6)		1.01	,	1.01
		1.31	1.28			1.156		1.232
		1.45	-1-					

computation cannot start with a flat meniscus, the numerical schemes were developed in [3] to begin the calculation with a hemispherical initial drop profile. For the simplified pressure history discussed there, it was sufficient to determine when the volume of fluid ejected from the nozzle reached that of a hemisphere and then use that as the starting time for the free surface flow calculation. However, with the numerically calculated pressure history to be used here, this simple procedure does not give usable results. The value calculated in this manner is too large, coming practically at the end of the positive part of the exit velocity history. It is still necessary to start the free surface calculation from a hemispherical initial shape, but the starting time has to be adjusted to allow a reasonable part of the exit velocity history to be used. Thus, a new parameter is introduced into the simulation, t_0 , the time delay from the

start of the pressure history to the time the free surface calculation can begin.

Four parameters are needed to fully specify the numerical simulation for a given fluid: Weber number W (or reference velocity V_0), driving pulse length $t_{\rm p}$, pressure pulse amplitude P_0 , and time to start the free surface calculation t_0 . This does not include the parameters required to determine the device geometry for the pressure history calculation. Since we are interested in comparing our calculations with a single experimental device, we only present results for the device shown in Figure 1. With the transducer design fixed, the major factor in determining the exit velocity history is pulse length $t_{\rm p}$, and hence it will be one of the parameters varied in our parameter study. The other major variable is the Weber number, which is determined by the surface tension of the fluid. Pressure pulse amplitude P_0 and initial time for the

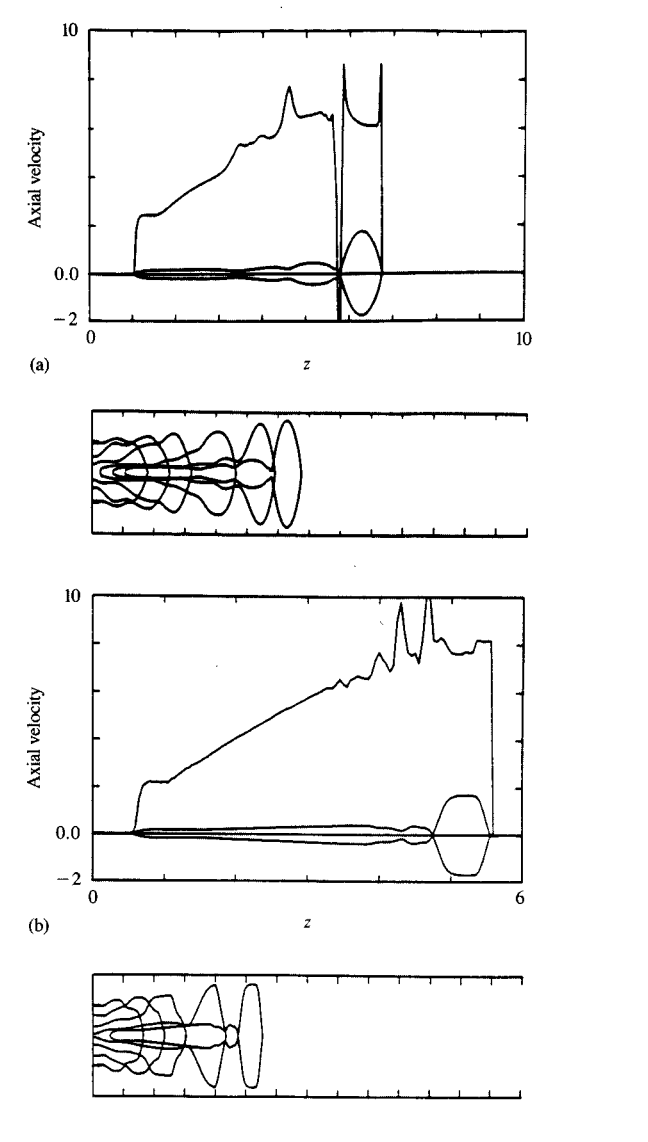


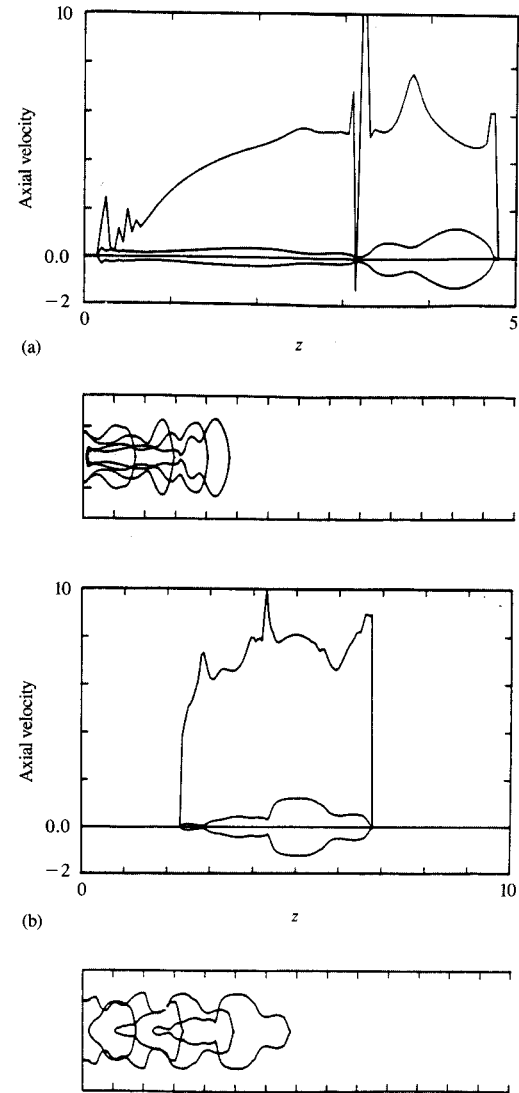
Axial velocity variation with position at satellite detachment calculated with (a) Scheme A for (i) $t_p = 15.0$, W = 5.0; (ii) $t_p = 20.0$, W = 5.0; (iii) $t_p = 25.0$, W = 1.0; and (b) Scheme B for (i) $t_p = 15.0$, W = 1.0; (iii) $t_p = 20.0$, W = 1.0; (iii) $t_p = 25.0$, W = 1.0.

free surface calculation will only be changed when it appears that a more reasonable simulation could be obtained with different values of these parameters. The circled data points on the velocity curves in Figures 7–10 show the points at which the free surface calculations begin.

With the use of the exit velocity histories shown in Figures 7–10, the drop formation sequences were computed for two Weber numbers and for both Scheme A and Scheme B, and they are also shown in these figures. The calculation parameters are summarized in **Table 3**, which gives the

times corresponding to the profiles in the figures. The times with the breakoff index correspond to the times at which the drops become detached from the nozzle, after which the driving velocity no longer has any effect on the calculation. To determine if the trailing satellites are moving faster or slower than the main drops, the velocity distributions in the drops were plotted at the breakup times, and they are plotted in Figure 11(a) for Scheme A and in Figure 11(b) for Scheme B. In all cases the satellites are moving slower than the main drop, but it was found that this can depend on the





Floring 42

Recalculation with $t_0 = 0.61$, $t_p = 25.0$, and W = 5.0 using (a) Scheme A and (b) Scheme B.

ELIGIUTE SAN

Recalculation with twice the driving pressure amplitude with $t_p = 10.0$, W = 5.0 using (a) Scheme A and (b) Scheme B.

time t_0 at which the free surface calculation is started. **Figure 12** shows a calculation for both schemes in which the starting time is changed from that in Figure 10 to the value $t_0 = 0.61$. **Figure 13** shows a calculation for both schemes in which the driving amplitude is twice that used in Figure 7.

• Discussion of numerical results and comparison with experiment

The main goal of the numerical simulation of the DOD ink jet is to be able to predict the shape of drops emitted from a

given device without experimentation; hence, we are mainly interested in showing that the behavior predicted is similar to the behavior observed experimentally. Also, since it is not possible to completely describe the device, certain assumptions are embodied in the simulation and their accuracy needs to be checked. One obvious difficulty with the simulation can be seen by comparing the experimental results in Figures 4 and 5 with the pressure and velocity histories in Figures 7–10. In Figures 4(a)-4(d) one sees that a second surge in volume occurs at $90 \mu s$. However, as shown

in Figures 7–10, the numerical simulation does not predict an arrival of a second positive pressure pulse and accompanying velocity surge before breakoff occurs.

The computations for a pulse length of 25 μ s shown in Figure 10 predict that for both Schemes A and B and for both Weber numbers there is a trailing satellite drop that is moving slower than the main drop. This is consistent with the notion that 25 μ s is not an optimal pulse length for this transducer chamber. The photographs in Figure 5(e) for water show a trailing satellite that eventually catches up and coalesces with the main drop. This suggests that a different starting time for the computation may be more appropriate. Figure 12 shows that Scheme A predicts a trailing satellite moving faster than the main drop, as seen from the velocity profile along the drop at breakup. Scheme B does not predict this, as shown in Figure 12, probably because it neglects radial inertia. The formation of satellites seems to be associated with waves moving along the drop that finally cause it to break up into several drops. Since Scheme B neglects radial inertia, which is very important to the modeling of oscillations, and the driving velocity is such that many oscillations are produced in the drop while it is attached to the nozzle, the predictions of Scheme B are not expected to be accurate in this case.

The computations for a pulse length of 20 μ s are shown in Figure 9. This pulse length is twice the fundamental tuning pulse length, hence the ejected drops are expected to have fewer satellites than for a pulse length of 25 μs. It is indeed seen that the trailing tails of the main drops are smaller in Figure 9 than in Figure 10, especially for Scheme A. Scheme B, however, still predicts a small trailing drop at the very end of the tail of the main drop. After we discovered from the experiment that the driving voltage needed to be increased to eject drops at a pulse length of 10 μ s, the experiment was repeated using this same increased voltage for a pulse length of 20 μ s with ethylene glycol, and the results are shown in Figure 4(d). This shows the same small drop on the end of the tail of the main drop as predicted by Scheme B. One of the properties of Scheme B is that when radial inertial effects do not play a major role in drop formation (say, when the driving velocity is relatively smooth), the lack of radial inertia appears to make the predicted behavior more like that of a more viscous fluid. That is, Scheme B appears to predict better the behavior of ethylene glycol than that of water. Scheme A, on the other hand, predicts the satellites found when water is used, which is also understandable, since the inclusion of radial inertia makes it possible to model the less viscous and hence more oscillatory water drops.

Figure 8 shows the computed results for a pulse length of $15 \mu s$, which is the most untuned pulse length studied for the transducer chamber in Figure 1. Consequently the two numerical schemes predict the largest satellites of all the pulse lengths studied. This agrees well with the experimental evidence. The ethylene glycol photographs in Figure 4(b)

show a very similar behavior of the drop tail, which actually forms a second drop almost the same size as the primary drop.

The $10-\mu s$ pulse length calculations are shown in Figure 7. This is the minimum tuned pulse length for our device. As suggested by the exit velocity profile, the drops ejected should move slower than those at the longer pulse lengths, and this is true for the experimental results as well. In fact, the same driving voltage used at the other pulse lengths did not eject a drop at this pulse length in the experiment. The drops predicted by the numerical schemes (when they were stable) had a very quick breakoff with no tail. This is similar to the experimental results, although the ethylene glycol showed a more pronounced tail during ejection. When the driving pressure, and hence the exit velocity for the simulation, was increased by a factor of two, Scheme A was able to predict a longer tail, as shown in Figure 13. However, Scheme B was unable to produce realistic results because of the large oscillations produced by the higher-amplitude driving velocity and the lack of radial inertia in the scheme.

4. Conclusions and suggestions for future work

It has been demonstrated for a particular DOD transducer design that the numerical simulation developed in our previous paper [3] can predict most of the behavior observed in the drop ejection experiment. It is true, however, that all of the parameters are not directly determined, and the undetermined ones can be adjusted so as to make the numerical predictions more closely model the experiment. It appears that with reasonable improvements the numerical simulator can be brought to the point where reliable predictions can be made.

The first improvement should be the inclusion of viscosity in a systematic way. The numerical model presented by Adams and Roy [4] included one term that appears in the Cosserat viscous jet equations derived by Green [8], but it did not include the other two. Indeed, since most of the inks are non-Newtonian, the numerical model should include viscoelastic effects as well. Such one-dimensional Cosserat jet equations have recently been presented by Bechtel et al. [9]. After that, the next improvement should probably be the development of a higher-order jet theory that can model the viscous flow profile inside the nozzle together with the jump conditions that occur at the nozzle exit. This is required in order to account for many of the effects observed to be associated with the profile relaxation just outside the nozzle on the free jet.

Acknowledgments

The first author, T. W. Shield, has consecutively held the Berkeley Fellowship and the National Science Foundation Graduate Fellowship. This work was also partially supported by an IBM Shared University Research Grant, Contract Proposal No. UCB-Eng. 5674.

References

- D. B. Bogy and F. E. Talke, "Experimental and Theoretical Study of Wave Propagation Phenomena in Drop-on-Demand Ink Jet Devices," *IBM J. Res. Develop.* 28, 314–321 (1984).
- J. D. Beasley, "Model for Fluid Ejection and Refill of an Impulse Drive Jet," J. Appl. Photog. Eng. 3, 78-82 (1977).
- 3. T. W. Shield, D. B. Bogy, and F. E. Talke, "A Numerical Comparison of One Dimensional Fluid Jet Models Applied to Drop-On-Demand Printing," J. Comp. Phys. 67 (1986).
- R. L. Adams and J. Roy. "A One-Dimensional Numerical Model of a Drop-On-Demand Ink Jet," J. Appl. Mech. 53, 193-197 (1986).
- J. Fromm, "A Numerical Study of Drop-On-Demand Jets," Proceedings of the Second International Colloquium on Drops and Bubbles, 1982, pp. 54–82.
- N. Bugdayci, D. B. Bogy, and F. E. Talke, "Axisymmetric Motion of Radially Polarized Piezoelectric Cylinders Used in Ink Jet Printing," *IBM J. Res. Develop.* 27, 171–180 (1983).
- 7. V. L. Streeter and E. B. Wylie, Fluid Transients, McGraw-Hill Book Co., Inc., New York.
- 8. A. E. Green, "On the Non-Linear Behavior of Fluid Jets," *Int. J. Eng. Sci.* **14**, 49-63 (1976).
- S. E. Bechtel, M. G. Forest, and D. B. Bogy, "A One-Dimensional Theory for Viscoelastic Fluid Jets, with Application to Extrudate Swell and Draw-Down Under Gravity," *J. Non-Newton. Fluid Mech.* 21, 273–308 (1986).

Received March 3, 1986; accepted for publication July 29, 1986

Thomas W. Shield University of California at Berkeley, Berkeley, California 94720. Mr. Shield is currently a Ph.D. candidate in the Department of Mechanical Engineering at the University of California, where he holds the National Science Foundation Graduate Fellowship. He received an M.S. from the University of California and a B.S. (with University Honors) from the University of Illinois, Department of Theoretical and Applied Mechanics.

David B. Bogy Department of Mechanical Engineering, University of California, Berkeley, California 94720. Dr. Bogy is a Professor of Applied Mechanics at Berkeley and since 1972 has been a consultant to the applied technology group at the IBM Research laboratory in San Jose. His current technical interests include work in elastic wave scattering and the mechanics of magnetic recording and printing technology. He received a B.A. in geology and mechanical engineering and an M.S. in mechanical engineering in 1959 and 1961, both from Rice University, Houston, Texas, and a Ph.D. in applied mathematics in 1966 from Brown University, Providence, Rhode Island. After postdoctoral work in elasticity at the California Institute of Technology, he joined the faculty of the University of California at Berkeley in 1967. Dr. Bogy is a member of the American Society of Mechanical Engineers and Sigma Xi.

Frank E. Talke *IBM Research Division, 5600 Cottle Road, San Jose, California 95193.* Dr. Talke joined IBM in 1969 at the San Jose Research laboratory and is currently on sabbatical leave as a visiting professor at the University of California at Berkeley. Previously he was manager of the device mechanics group in the applied science complex in San Jose, where he initiated the work on drop-on-demand ink jet technology. Prior to that, he studied the mechanical aspects of magnetic recording technology. He attended the University of Stuttgart, Germany, where he received a Diplom-Ingenieur degree (M.S.) in mechanical engineering in 1965, and the University of California at Berkeley, where he received a Ph.D. in mechanical engineering in 1968.